Improvement of NO$_2$ Sensing Properties in Pd Functionalized Reduced Graphene Oxides by Electron-Beam Irradiation

Myung Sik Choi[1], Ali Mirzaei[2], Jae Hoon Bang[1], Wansik Oum[1], Sang Sub Kim[3]* and Hyoun Woo Kim[1,4]*

[1] Division of Materials Science and Engineering, Hanyang University, Seoul, South Korea, [2] Department of Materials Science and Engineering, Shiraz University of Technology, Shiraz, Iran, [3] Department of Materials Science and Engineering, Inha University, Incheon, South Korea, [4] The Research Institute of Industrial Science, Hanyang University, Seoul, South Korea

Herein, we present the effect of electron-beam irradiation (EBI) on the gas-sensing properties of Pd-functionalized reduced graphene oxide (RGO). Scanning electron microscopy, transmission electron microscopy, and X-ray photoelectron spectroscopy were used to characterize the synthesized products. The samples were irradiated using electron beams at doses of 0 (Pd-RGO-0), 100 (Pd-RGO-100), and 500 kGy (Pd-RGO-500), and the NO2 gas-sensing properties were investigated. It was found that irradiation by electron beams has a critical effect on the gas-sensing properties of the samples, and the Pd-RGO-500 sensor showed the highest response to NO$_2$ gas. In particular, the response of the unirradiated sensor and the sensor irradiated at doses of 100 and 500 kGy to 10 ppm NO$_2$ were 1.027, 1.045, and 1.047, respectively. The response times of Pd-RGO-0, Pd-RGO-100, and Pd-RGO-500 to 10 ppm NO$_2$ gas were 389, 335, and 345 s, respectively. The corresponding recovery times for these sensors were 808, 766, and 816 s, respectively. The increased numbers of oxygen functional groups and high-energy defects were the main reasons for the increased gas response. This study will eventually lead to increased performance levels of RGO-based sensors that use EBI, as this technology can introduce changes into materials in a non-contact, clean, and powerful manner.

Keywords: reduced graphene oxide, electron-beam irradiation, Pd nanoparticles, gas sensor, NO$_2$ gas
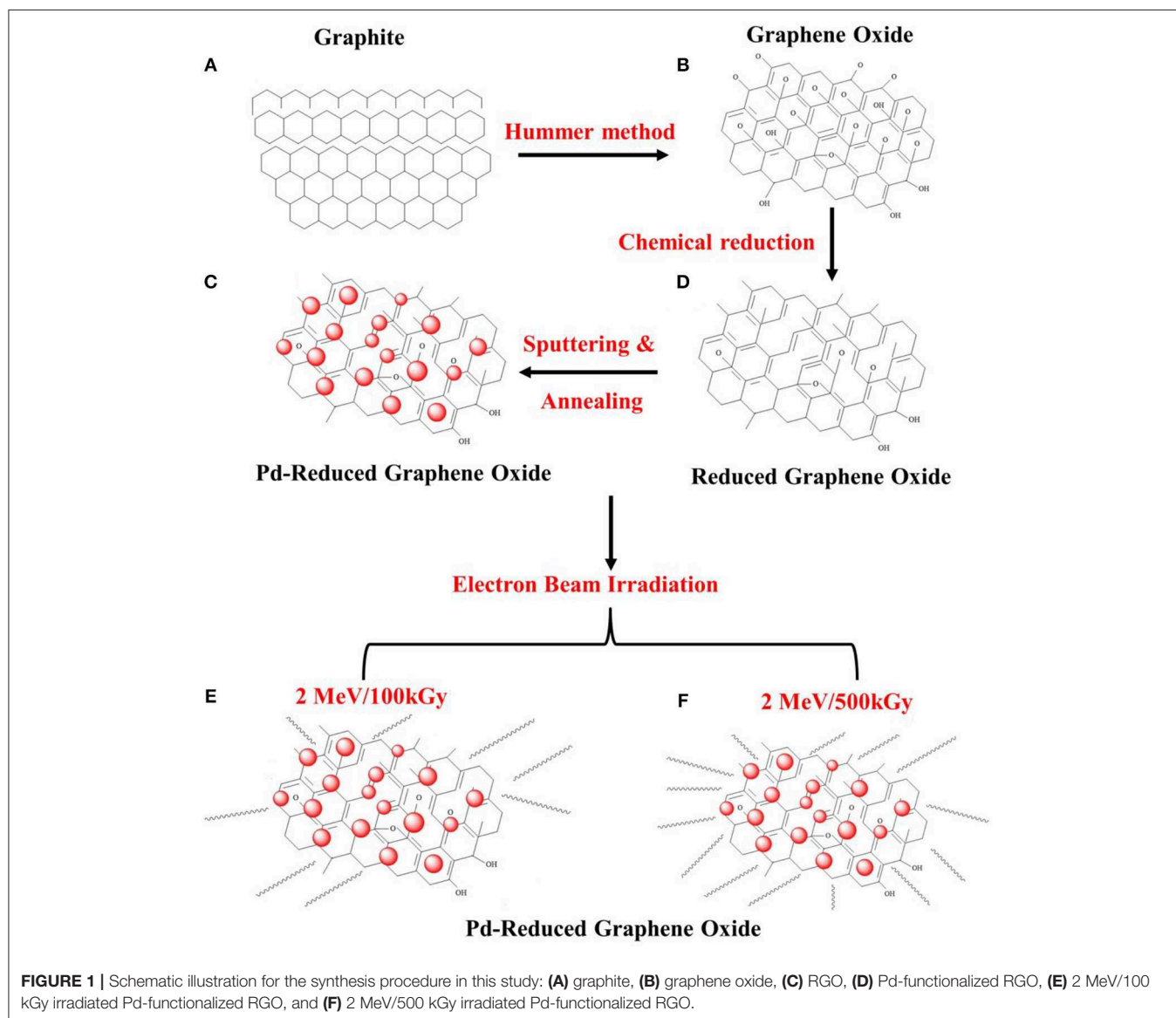
INTRODUCTION

Metal oxide gas sensors at present are among the most important sensing instruments for the detection of gases (Mirzaei et al., 2016; Kim et al., 2018) and humidity (Su et al., 2017). In spite of their remarkably high sensitivity, short response, and quick recovery times, they can exhibit poor stability and high sensing temperatures, thus limiting their wider use (Choi et al., 2014).

This has motivated researchers to develop alternative materials, especially those that may decrease the sensing temperature. Carbon-based materials are suitable candidates for gas sensors due to their large surface area, thermal stability, and extraordinary electrical conductivity (Uddin and Chung, 2014). Among the carbon materials developed thus far, graphene is a rising star with the abovementioned attributes, and it has been extensively investigated in different areas of science and technology (Banhart et al., 2010; Terrones et al., 2012). A converted form of graphene known as reduced graphene oxide

(RGO) has properties similar to those of pristine graphene, but a difference lies in the presence of certain oxygen-containing functional groups in RGO, even after a reduction process (Paredes et al., 2008). These oxygen-functional groups render RGO hydrophilic making soluble in water and many other solvents. This solubility allows RGO to be uniformly deposited onto any substrate (Craciun et al., 2013). Furthermore, chemical reduction for the synthesis of RGO is perceived to be a very economical and efficient approach, as it can produce RGO on a large scale from cost-effective natural graphite (Pham et al., 2011). Thus, due to such an inexpensive means of production and the availability of large quantities, RGOs are commercially available at reasonable prices, making them extremely attractive materials for sensing studies. For example, Du et al. (2019), reported the NH_3 sensing properties of RGO and proposed a model for its sensing behavior.

RGO sheets have a tendency to agglomerate through van der Waals forces between adjacent layers. As a result, this greatly increases the internal resistance and thus limits the broader application of this material. However, RGO-based composites are effective when used to prevent the re-stacking of RGOs to improve its properties (Lu et al., 2011).

The utilization of nanomaterials has explosively increased with a great amount of work reported (Jung et al., 2016; Karimipour and Molaei, 2016; Kiani et al., 2016; Kim J. et al., 2016; Kim T. U. et al., 2016); Lee et al., 2016; Meang et al., 2016; Tola et al., 2016; Truong and Park, 2016). Recently, nanocomposites based on RGO have been synthesized through the decoration of different NPs on graphene oxide (GO) or RGO, which have numerous applications in lithium ion batteries (Chen et al., 2015), surface-enhanced Raman spectroscopy (Huang et al., 2015), sensors (Bas, 2015), photo-catalysts

FIGURE 1 | Schematic illustration for the synthesis procedure in this study: (A) graphite, (B) graphene oxide, (C) RGO, (D) Pd-functionalized RGO, (E) 2 MeV/100 kGy irradiated Pd-functionalized RGO, and (F) 2 MeV/500 kGy irradiated Pd-functionalized RGO.

(Yan et al., 2014; Hareesh et al., 2016), and others. In the research on gas sensing, one advantage of nanoparticle decoration is that a noble metal can be used to enhance the gas responses of sensors by chemical and electrical sensitization (Lin and Hsu, 2013; Zhang et al., 2018). For example, Tran et al. (2014) synthesized RGO/Ag with enhanced NH_3 sensing properties relative to pristine RGO at room temperature. Also, Su et al. (2016) used RGO-polyethylene oxide film for detection of toluene at room temperature.

EBI has become extensively used in a variety of applications, such as the cleaning and sterilization of medical tools and the synthesis of different materials and nanocomposites (Hareesh et al., 2016). This is mainly due to the environmentally friendly characteristics and cost-effectiveness of this method. It has also been utilized for the synthesis and modification of carbon-based materials such as carbon nanotubes (Smith and Luzzi, 2001) and fullerenes (Krasheninnikov and Banhart, 2007). The modification of its properties principally results from the creation of defects by EBI, which can greatly affect the final properties of materials, such as the gas-sensing properties (Kwon et al., 2014).

Although there are some reports of the gas-sensing properties of noble-metal-loaded RGO sensors (Yu et al., 2013), to the best of our knowledge, reports about the effect of EBI on the sensing behavior of RGO-based sensors are rare. NO_2 is a highly toxic gas, and exposure causes lung irritation and decreased fixation of oxygen molecules on red blood corpuscles. Furthermore, it is one of the main causes of acid rain (Brunet et al., 2001). Moreover, with increasing industrialization, the release of NO_2 and its derivatives has significantly threatened human health and public security (Su et al., 2018). Thus, the development of gas sensors for the detection of NO_2 is extremely urgent. In this study, we investigate the effects of EBI on the NO_2 sensing behavior of Pd-functionalized RGO sensors. To do this, RGOs were prepared by the chemical reduction of GO and a Pd layer was subsequently deposited by a sputtering process. The final step was thermal annealing. The effects of EBI on the physical/chemical properties of RGOs were investigated and the NO_2 sensing properties of irradiated sensors were compared with those of unirradiated samples.

EXPERIMENTAL

Sample Preparation

Graphite was used as a starting material and GO was prepared by Hummer's method (Hummers and Offeman, 1958) with the same procedure in the previous report (Kwon et al., 2014). The oxidation process of 1 g of graphite was accomplished by stirring with 46 ml of H_2SO_4 and 12 g $KMnO_4$ in the presence of 12 g H_3PO_4, which acted as strong oxidizing agents. The purpose of this step was to increase the interlayer distance between the graphite packed layers to facilitate exfoliation and separation of graphene sheets in the final step. After repeating the washing and filtration several times, a very fine brown powder was allowed to dry in a vacuum oven. By adding hydrazine monohydrate and subsequently heating at 150°C in an oil bath, the exfoliated GO nanosheets were transformed to RGO. Re-dispersion in dimethylformamide (DMF) by sonication led to the formation of homogenous RGO suspension. Subsequently, by coating the
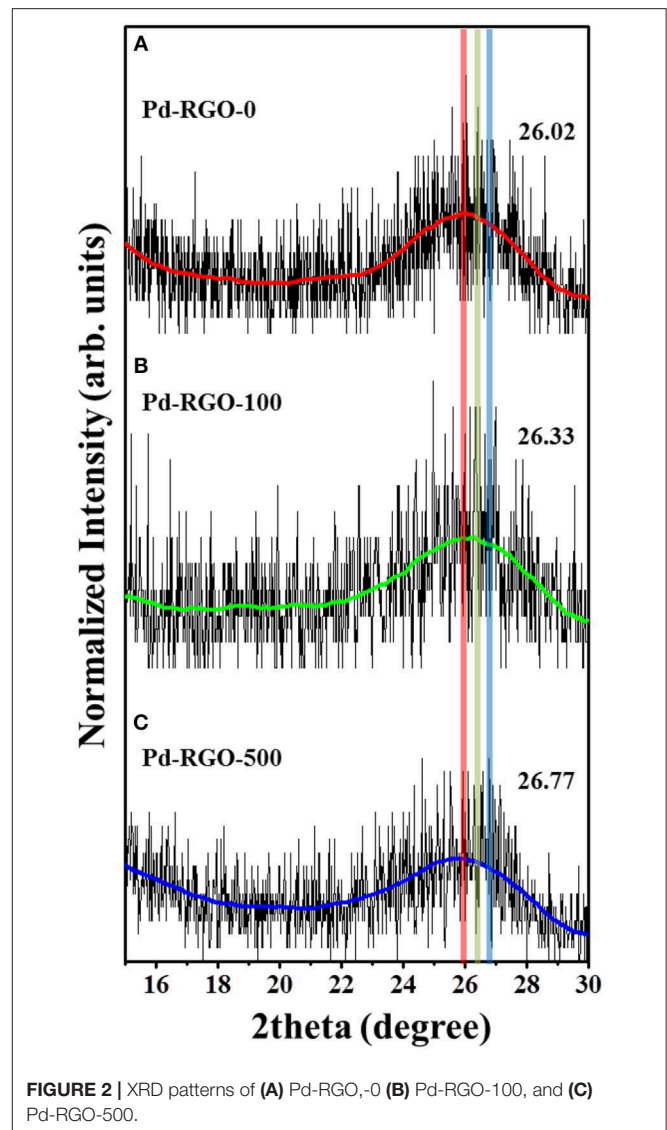
FIGURE 2 | XRD patterns of **(A)** Pd-RGO,-0 **(B)** Pd-RGO-100, and **(C)** Pd-RGO-500.

RGO suspension on quartz substrates, the RGO films were prepared. Before annealing, they were heated at 250°C for 3 h to remove the moisture and annealing was conducted at 1100°C for 30 min. All heating and cooling processes were carried out with a gas flow of (Ar + H_2) at a rate of 100 sccm. The thickness of the RGO films were in the range of 100–300 nm.

To coat the Pd layer, a turbo sputter coater with a Pd target (Emitech K575X, Emitech Ltd., Ashford, Kent, UK) was used at room temperature. In the Ar plasma sputtering process, deposition time and DC sputter current were kept to 5 s and 65 mA, respectively. As a result, the Pd layer with a thickness of 3 nm was deposited on the RGOs. Following this, the samples were annealed at 700°C for 30 min, in the presence of Ar gas with flow rate of 2,000 sccm. This resulted in the creation of Pd NPs as isolated islands dispersed on the surface of RGO that are beneficial for gas sensing applications.

The Pd-functionalized RGO films were irradiated with an electron beam in air at room temperature in the absence of

a vacuum system. The ELV-8 electron accelerator (EBTech, Daejeon, Korea) was used to deliver an accelerating energy of 2 MeV with doses of 100 and 500 kGy, a beam current of 1 mA, and a pulse duration of 400 ps. Accordingly, un-irradiated Pd-functionalized RGO, Pd-functionalized RGO irradiated at 100 kGy and Pd-functionalized RGO irradiated at 500 kGy gas sensors, were coded as Pd-RGO-0, Pd-RGO-100, and

Pd-RGO-500, respectively. **Figure 1** schematically shows the steps of the synthesis procedure in this study.

Characterization

Morphological features of the Pd-functionalized RGOs samples were examined using a scanning electron microscope (SEM, JEOL, JSM 5900 LV, Japan) and transmission electron microscopy
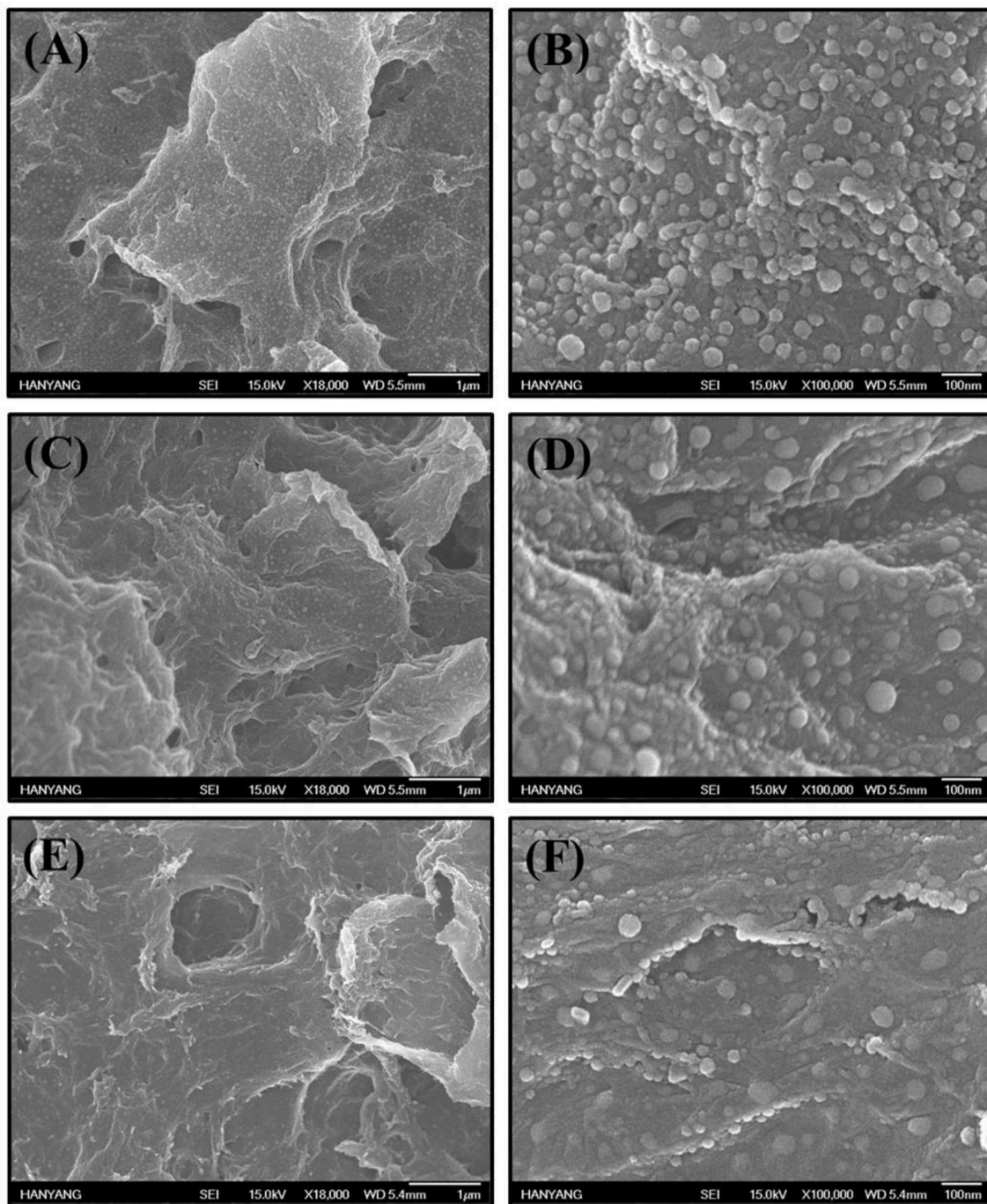
FIGURE 3 | (A,B) SEM images of Pd-RGO-0, **(C,D)** Pd-RGO-100, and **(E,F)** Pd-RGO-500.

(HR-TEM) with a TECNAI 20 microscope operated at 200 kV and coupled with an energy dispersive spectrometer (EDS). X-ray diffraction (XRD) patterns were recorded using Cu Kα (λ = 1.541 Å) radiation (Rigaku, Japan) to study structure and phase formation of samples in the Figures. X-ray photoelectron spectroscopy (XPS, VG Multilab ESCA 2000 system, UK) was employed to analyze the elemental compositions, by means of a monochromatized Al Kα x-ray source (hv = 1486.6 eV) at the Korean Basic Science Institute (KBSI). The binding energies obtained from the XPS analysis were corrected for specimen charging by referencing the C1s line to 284.5 eV. Raman scattering under an Ar-ion laser source (532 nm) was performed using a Horiba Jobin-Yvon LabRam HR Evolution system, equipped with a confocal microscope (100× microscope objective lens).
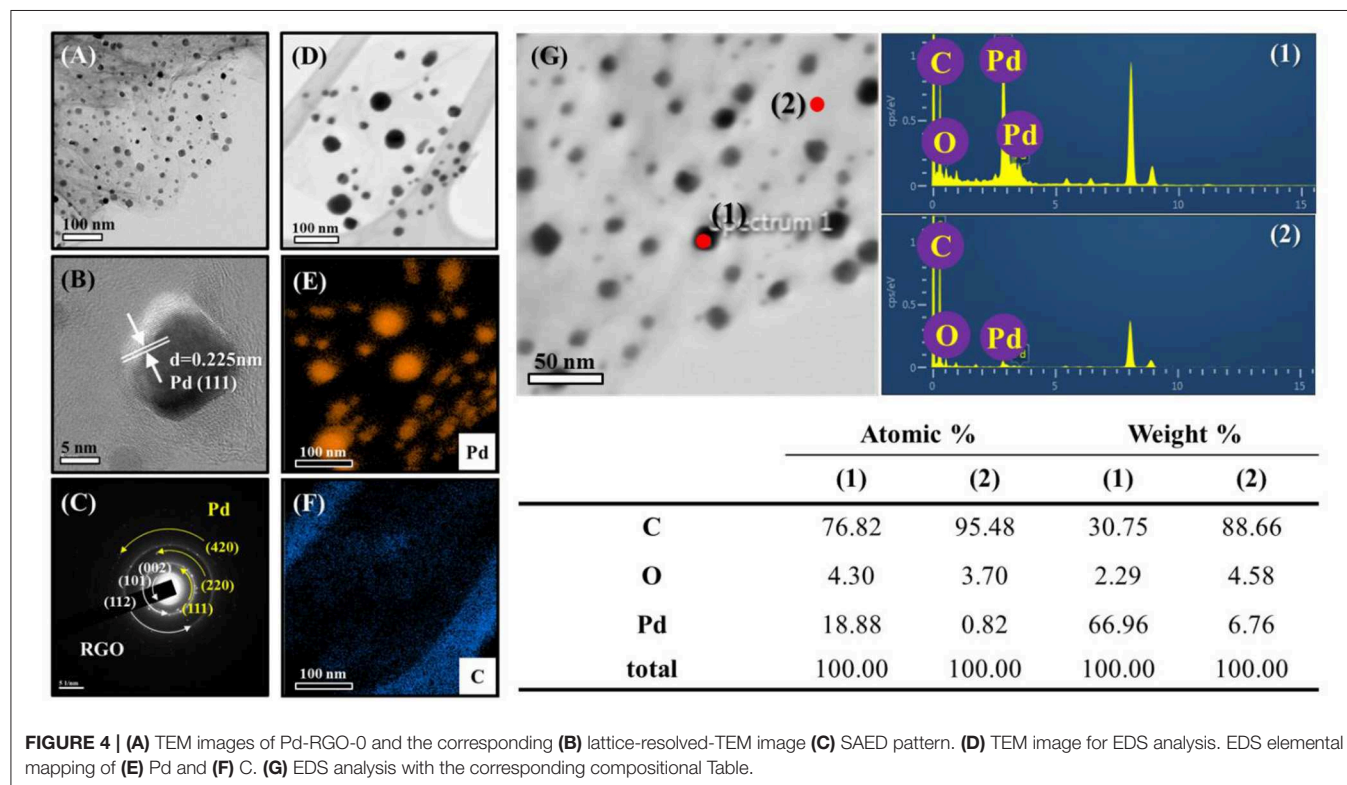
Gas Sensing Characterization

For sensing studies, Ni/Au double-layer electrodes were used in which Ni (∼200 nm thickness) and Au (∼50 nm thickness) were sequentially deposited via sputtering by an interdigital electrode mask. The sensor was placed in a horizontal-type tube furnace that was connected to an electrical measuring system (Keithley 2400) interfaced with a computer. The tube furnace was evacuated to 10^{-3} Torr by a rotary pump. The gas concentration was controlled by changing the mixing ratio of the target gas and dry air through mass flow controllers, with the total flow rate fixed at 100 sccm to avoid any possible variation in sensing properties. NO_2 concentration was adjusted to 10 ppm. During the recovery period, the system was purged at a flow rate of 100 sccm with ambient dry air. The sensing setup is similar to that used previously by our research group (Kwon et al., 2017). The change of resistance was measured in the presence of NO_2 at room temperature inside the chamber. The sensor response was defined as $R = R_a/R_g$. The response and recovery times were defined as the times taken for the resistance to change by 90% on exposure to the target gas (NO_2) and air, respectively.

RESULTS AND DISCUSSIONS

Structural, Morphological, and Chemical Analyses

XRD was performed to study the phase formation characteristics of the samples. **Figure 2** compares the positions of the (002) XRD peaks of all samples. For Pd-RGO-0, Pd-RGO-100, and Pd-RGO-500, the peak positions of the (002) plane are located at 26.02°, 26.33°, and 26.77°, respectively, which is in accordance with the (002) plane of graphite as a raw material (Yeung et al., 2008). It has been reported that the interplanar spacing is proportional to the degree of oxidation (Xu et al., 2011) and the compressive residual strain (Babitha et al., 2014). Due to the generation of oxygen-functional groups between the layers, the d-spacing of RGO can be increased and the presence of strain will result in a decrease in the interplanar spacing (Xu et al., 2011; Babitha et al., 2014). As observed here, the peak positions are shifted to higher angles after irradiation with an electron beam, resulting in a slight decrease in the lattice spacing. This decrease is in accordance with Bragg's law: 2dsinθ = nλ, where d is the

	Atomic %		Weight %	
	(1)	(2)	(1)	(2)
C	76.82	95.48	30.75	88.66
O	4.30	3.70	2.29	4.58
Pd	18.88	0.82	66.96	6.76
total	100.00	100.00	100.00	100.00

FIGURE 4 | (A) TEM images of Pd-RGO-0 and the corresponding **(B)** lattice-resolved-TEM image **(C)** SAED pattern. **(D)** TEM image for EDS analysis. EDS elemental mapping of **(E)** Pd and **(F)** C. **(G)** EDS analysis with the corresponding compositional Table.
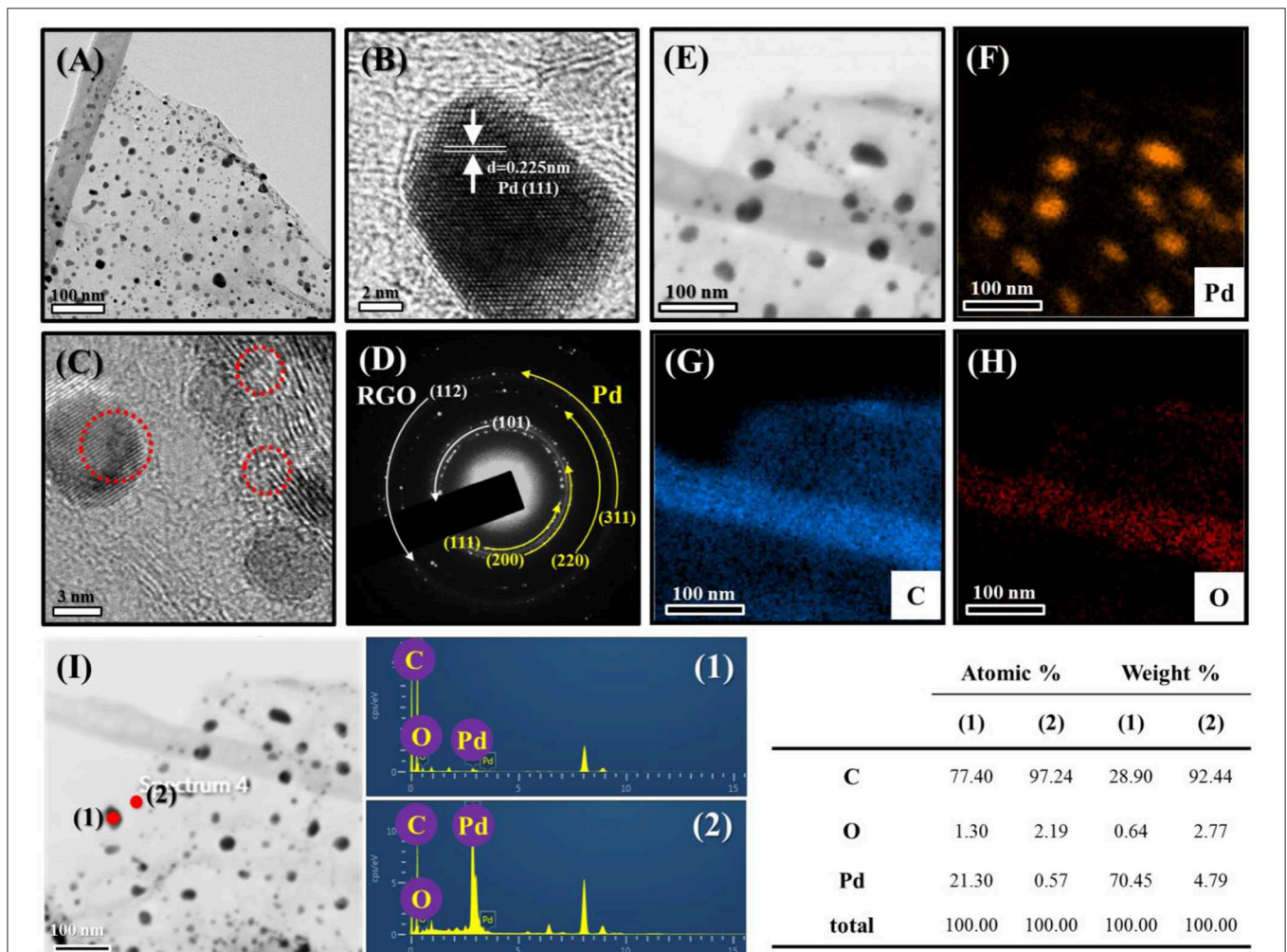
interplanar spacing, θ is the angle of diffraction, and λ is the wavelength of the X-rays (0.1541 nm). The small decrease in the lattice spacing can be attributed to the compressive residual strain caused by electron irradiation. The electron irradiation creates ion vacancies, non-stoichiometry, and surface defects, which can introduce strain into the lattice (Babitha et al., 2014). Similarly Chen et al. investigated the structural changes in GO caused by an electron beam with an absorbed dose of 500 kGy, finding that the interlayer spacing of GO was decreased.

SEM images are presented in **Figure 3**, showing that Pd NPs are uniformly distributed on the RGO surfaces. **Figures 3A,B** show low- and high-magnification SEM images of Pd-RGO-0. The un-irradiated sample has a relatively smooth surface with the presence of Pd NPs. **Figures 3C–F** show SEM images of Pd-RGO-100 and Pd-RGO-500, respectively. After irradiation with an electron beam at a dose of 100 kGy, the surface appeared slightly rough. Under a high

dosage of electron beams (500 kGy), the surfaces become rougher and more distorted. It was assumed that when RGO is irradiated by an electron beam at a high dose, its morphology changes.

The morphologies and structures of the samples were also subjected to a TEM analysis. **Figure 4A** shows a TEM image of Pd-RGO-100. Transparent RGO sheets functionalized by the fine dark NPs of Pd are easily observed in this image. The sizes of the Pd NPs ranged from 5 to 20 nm. **Figure 4B** shows an HRTEM image of the lattice fringe with a spacing of 0.225 nm, which is likely related to the (111) plane of Pd with a face-centered cubic structure. The selected-area electron diffraction (SAED) pattern of the sample is presented in **Figure 4C**, where the ring patterns of the (111), (220), and (420) planes of Pd and the (002), (101), and (112) planes of RGO are clearly observed, indicating the presence of both Pd and RGO. Elemental maps in **Figure 4D** are presented in **Figures 4E,F** for Pd and C, respectively, providing further evidence of the presence of

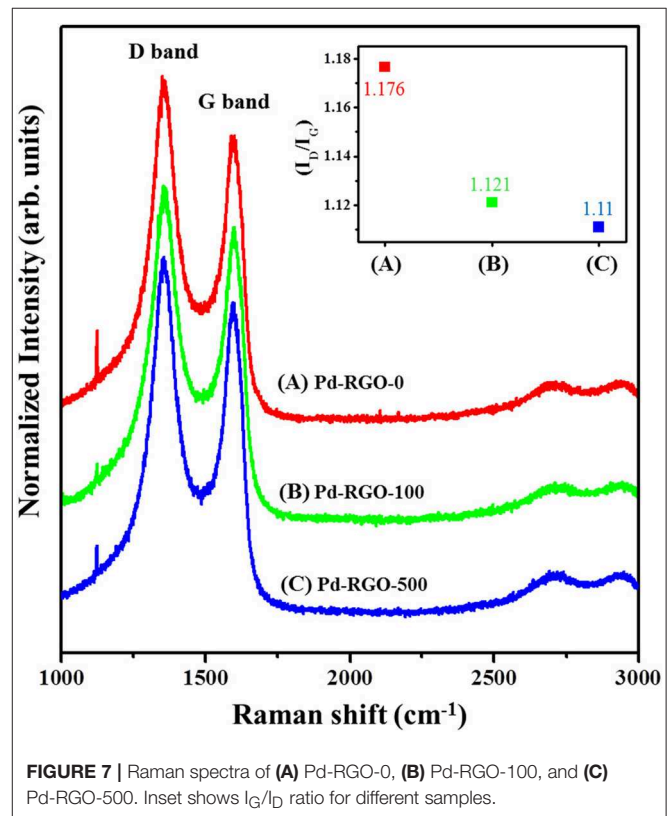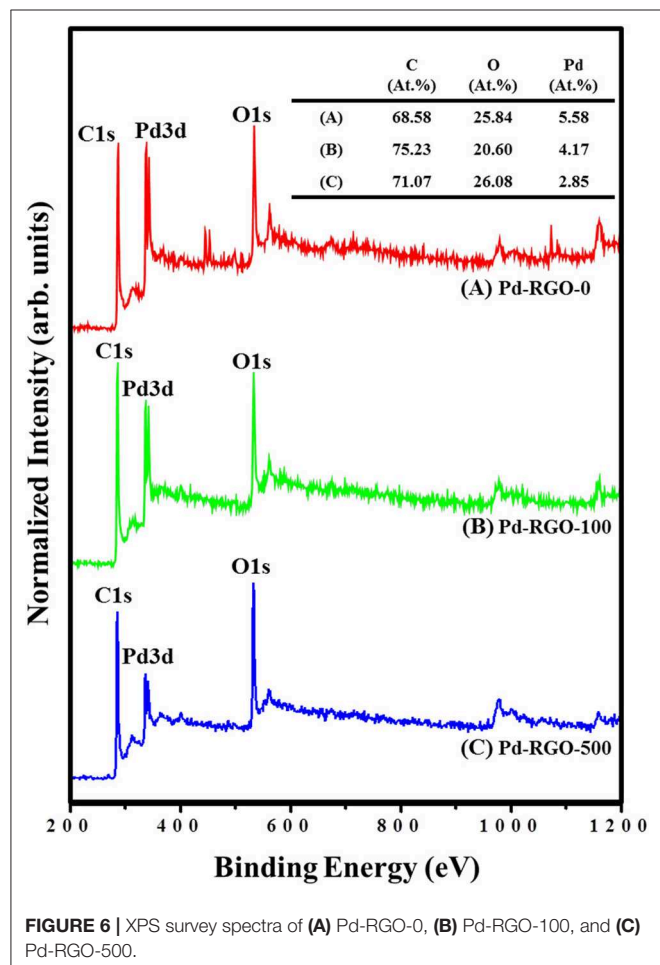|	Atomic %		Weight %	
	(1)	**(2)**	**(1)**	**(2)**
C	77.40	97.24	28.90	92.44
O	1.30	2.19	0.64	2.77
Pd	21.30	0.57	70.45	4.79
total	100.00	100.00	100.00	100.00

FIGURE 5 | (A) TEM images of Pd-RGO-500 and the corresponding **(B)** lattice-resolved-TEM image. **(C)** TEM image indicating defects in the sample. **(D)** SAED pattern. **(E)** TEM image for EDS analysis. EDS elemental mapping of **(F)** Pd, **(G)** C, and **(H)** O. **(I)** EDS analysis with the corresponding compositional Table.

fine and disperse Pd NPs in a matrix of carbon. According to the corresponding chemical analysis by EDS, the dark points correspond to Pd, whereas the transparent point is rich in carbon (**Figure 4G**). Furthermore, it can be seen that there are no other impurities in the sample, demonstrating the high purity of the starting materials and the appropriate synthesis procedure used. The Pd-RGO-500 underwent the same analysis. **Figures 5A,B** show TEM and HRTEM images of the samples, respectively, in which the presence of Pd NPs in a carbon matrix is evident. **Figure 5C** shows an HRTEM image, where the defects due to irradiation with high-energy electron beams are denoted by red circles in the image. If the kinetic energy transferred to the RGO is greater than a threshold value for bond-breaking, the carbon atoms will be displaced in a sub-picosecond time, generating a vacancy of displacement from their regular sites [37]. In the SAED pattern (**Figure 5D**), the rings correspond to the (111), (200), (220), and (311) planes of Pd and the (101) and (112) planes of carbon. The results of the EDS elemental mapping of the TEM image in **Figure 5E** are given in **Figures 5F–H** for Pd, C, and O, respectively. Some traces of oxygen were observed, likely due to atmospheric oxygen and the oxygen-functional groups of RGO. A precise chemical analysis of the

sample is shown in **Figure 5I**, with elements of Pd, C and O apparent.

As a surface-sensitive technique, XPS can only detect elements at a depth of no more than 10 nm (Huo et al., 2014), and a large analysis area will result in the simultaneous analysis of elements in the sample. **Figures 6A–C** show the XPS survey spectra of Pd-RGO-0, Pd-RGO-100, and Pd-RGO-500, respectively. In the survey-scan XPS spectra, the peaks at approximately 285.5, 335.5 and 534.0 eV correspond to the C1s, Pd3d, and O1s core levels, respectively (Brun et al., 1999). The atomic percentage (at.%) of each element was calculated from the wide-scan spectra, and the results are summarized in **Figure 6**. In the Pd-RGO-0, the atomic concentration ratios of C, O, and Pd were calculated and found to be approximately 68.58, 25.84, and 5.58%, respectively. For, Pd-RGO-100, the atomic concentration ratios of C, O, and Pd were changed to 75.23, 20.60, and 4.17%, respectively, while for the Pd-RGO-500 sample, the corresponding ratios were 71.07, 26.08, and 2.85%, respectively. It appears that after irradiation at 100 kGy, some oxygen defects are created, which is in accordance with the results of Know et al. for GO (Kwon et al., 2016). Kang et al. also reported oxygen decreases after irradiation with electron beams in GO (Kang et al., 2015). In another study, Jin et al. reported a similar trend for RGO irradiated with electron beams (Jin et al., 2013). However, after irradiation with 500 kGy, numerous defective sites can be created, which eventually can adsorb some of the oxygen from the ambient environment. In other words, the RGO is partially oxidized after irradiation with a dose of 500

FIGURE 6 | XPS survey spectra of **(A)** Pd-RGO-0, **(B)** Pd-RGO-100, and **(C)** Pd-RGO-500.

FIGURE 7 | Raman spectra of **(A)** Pd-RGO-0, **(B)** Pd-RGO-100, and **(C)** Pd-RGO-500. Inset shows I_G/I_D ratio for different samples.

kGy, which is the reason for the increased oxygen content in this sample.
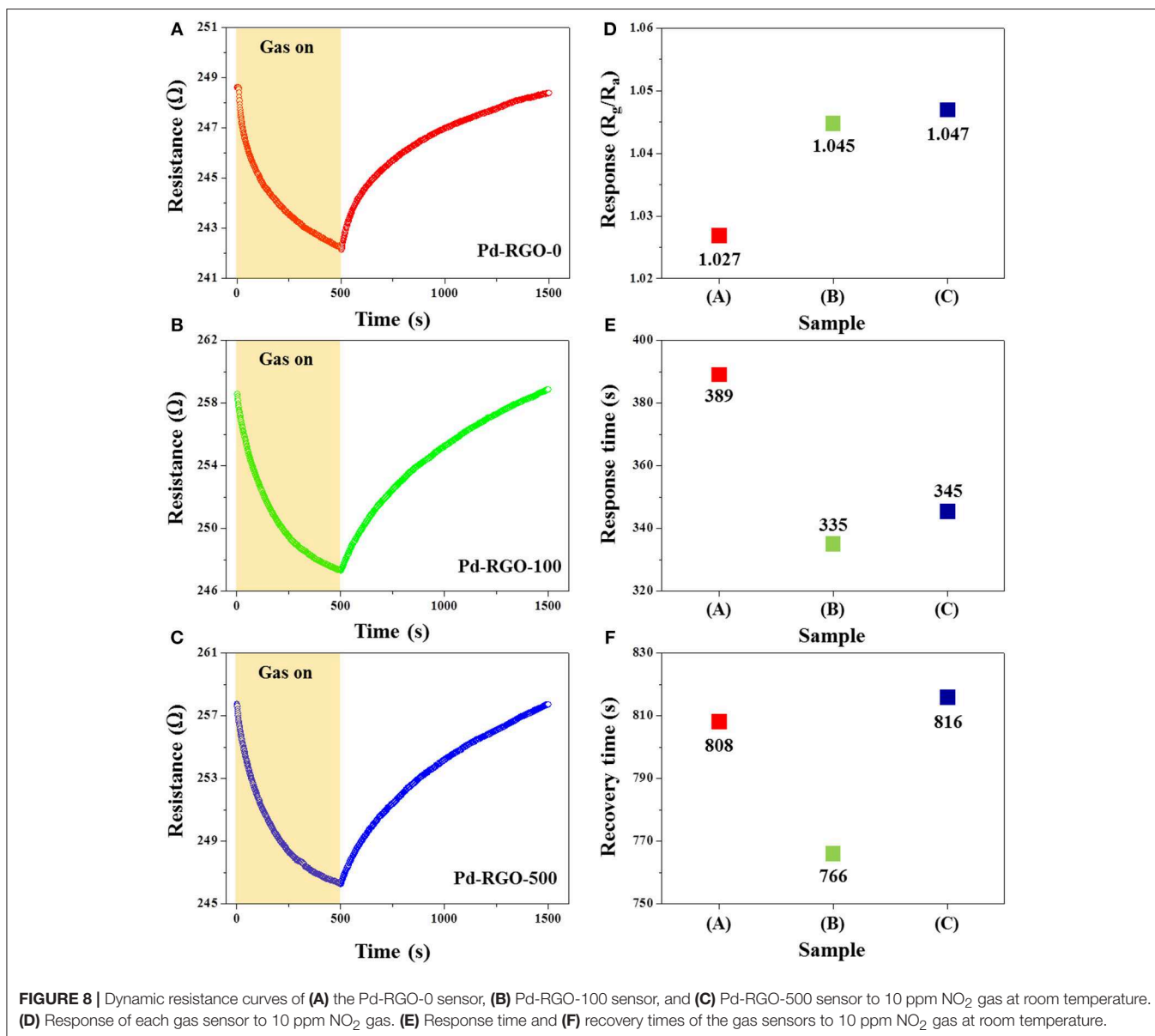
The Raman spectra of the different gas sensors are shown in **Figure 7**. The two peaks around ~1,350 and ~1,580 cm^{-1} are present in all samples, known as the D peak and G peak, respectively. The G band corresponds to the E_{2g} mode, which exists for all sp^2 carbon systems. Unlike the G band, the D band is due to the presence of defects. The Tuinstra-Koenig relation, which is the ratio of the intensity of the D and G peaks (I_D/I_G), represents the disorder of the material. A greater ratio indicates more disorder of the RGO (Mirzaei et al., 2018).

The I_D/I_G values of Pd-RGO-0, Pd-RGO-100, and Pd-RGO-500 gas sensors were 1.176, 1.121, and 1.11, respectively. It can be assumed that during the reduction of graphite, many defects, including oxygen and carbon vacancies or the incomplete
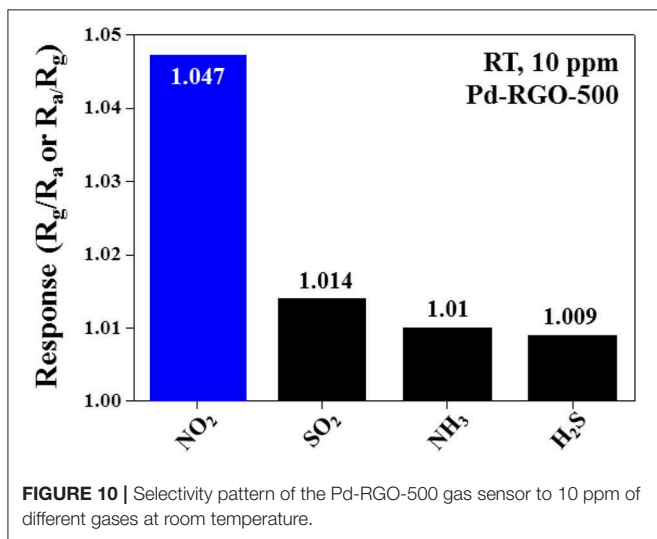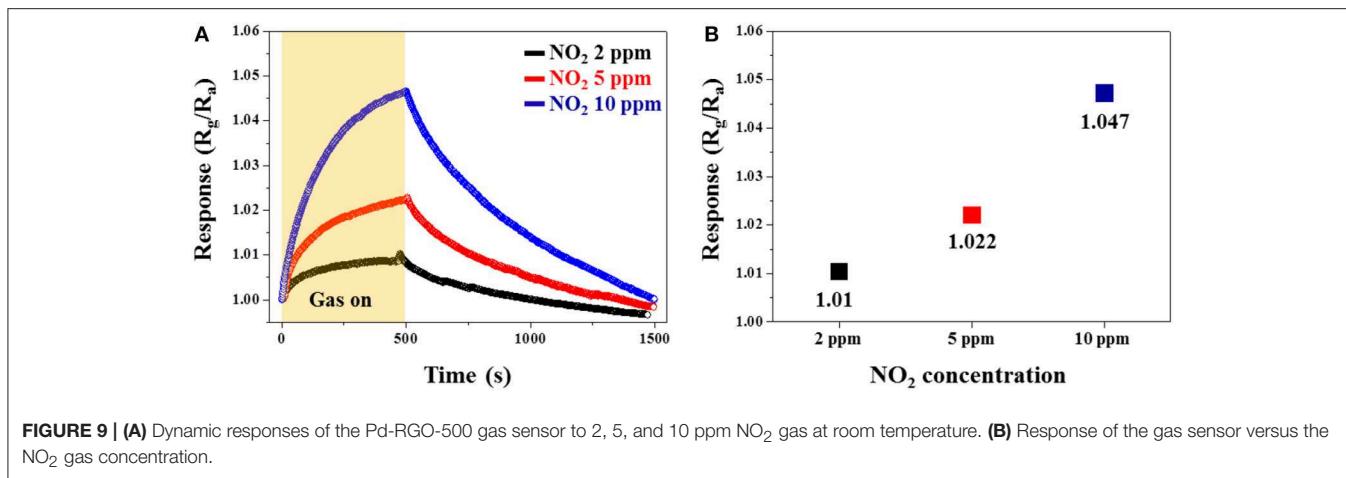
removal of epoxy/oxygenated functional groups, are generated in the RGO. During EBI, the removal of oxygen functional groups is accompanied by the creation of more oxygen defects. At the same time, the RGO is oxidized, which decreases the number of oxygen defects. The sample irradiated with the higher dose initially generated higher amounts of defects; subsequently in air, more oxygen species were adsorbed onto the active defects of RGO, thus decreasing the number of active defects for the sample irradiated at the higher dose.

Gas-Sensing Studies

The NO$_2$ gas-sensing properties of the RGO-based sensors were studied at room temperature. **Figures 8A–C** show the dynamic resistance changes of the gas sensors for 10 ppm of NO$_2$ gas. In all cases, the resistance was decreased after the introduction of

FIGURE 8 | Dynamic resistance curves of **(A)** the Pd-RGO-0 sensor, **(B)** Pd-RGO-100 sensor, and **(C)** Pd-RGO-500 sensor to 10 ppm NO$_2$ gas at room temperature. **(D)** Response of each gas sensor to 10 ppm NO$_2$ gas. **(E)** Response time and **(F)** recovery times of the gas sensors to 10 ppm NO$_2$ gas at room temperature.

FIGURE 9 | (A) Dynamic responses of the Pd-RGO-500 gas sensor to 2, 5, and 10 ppm NO_2 gas at room temperature. **(B)** Response of the gas sensor versus the NO_2 gas concentration.

FIGURE 10 | Selectivity pattern of the Pd-RGO-500 gas sensor to 10 ppm of different gases at room temperature.

has high energy, the ratio of high-energy to low-energy binding sites is increased in the sensor irradiated at 500 kGy. Therefore, detachment of NO_2 molecules requires more time. Similarly, Yang et al. reported a slow desorption rate of NO_2 gas compared to the fast adsorption rate as a result of defective sites on the surface in pristine graphene (Yang et al., 2013). The longer response time may also be related to the more tortuous structure of the irradiated samples. With the assumption of a Knudsen flow for NO_2 diffusion, the diffusion coefficient of NO_2 gas can be determined by the following equation (Huang et al., 2010):

$$D_K = \frac{\varepsilon d}{3\tau} \left(\frac{8RT}{\pi M} \right)^{0.5}. \tag{1}$$

Here, D_K is the Knudsen diffusion coefficient in a porous medium, ε is dimensionless porosity, τ is the dimensionless tortuosity, d is the pore diameter, R is the gas constant, T is the temperature, and M is the molar mass. From the above equation, NO_2 diffusion is directly proportional to the porosity and pore diameter, whereas it is inversely proportional to the tortuosity of the sensor. As EBI can generate more complex channels and pores within the structure, more time is required for NO_2 molecules to be completely desorbed from the sensor.

Figure 9A shows the dynamic response curves of the Pd-RGO-500 gas sensor to 2, 5, and 10 ppm NO_2 gas. As shown in **Figure 9B**, the response of the gas sensor to 2, 5, and 10 ppm NO_2 gas is 1.01, 1.022, and 1.047, respectively. **Figure 10** shows the selectivity histogram of the Pd-RGO-500 gas sensor irradiated at a dose of 500 kGy. As observed, the response of the gas sensor to 10 ppm NO_2, SO_2, NH_3, and H_2S gases is 1.047, 1.014, 1.01, and 1.009, respectively.

When sensors are placed in an open air environment, oxygen molecules adsorb on their surfaces and trap the electrons from the conduction band of the sensing layer, leaving oxygen absorbents (O^{2-}) at room temperature (Choi et al., 2011). It is noteworthy that oxygen molecules can easily be adsorbed onto the oxygen vacancies of RGO.

$$O_2 \, (gas) + e^- \rightarrow O^-_{2(ads)} \tag{2}$$

NO_2 gas, demonstrating the p-type behavior of the gas sensors. This result is in good agreement with the findings of a previous work (Wang et al., 2012). **Figure 8D** shows the response of all gas sensors to 10 ppm NO_2 gas, indicating that the responses of Pd-RGO-0, Pd-RGO-100, and Pd-RGO-500 sensors were 1.027, 1.045, and 1.047, respectively. It was clearly observed that the order of increase in the gas sensor responses is as follows: Pd-RGO-500 > Pd-RGO-100 > Pd-RGO-0. As shown in **Figures 8D,E**, the response times of Pd-RGO-0, Pd-RGO-100, and Pd-RGO-500 to 10 ppm NO_2 gas were 389, 335, and 345 s, respectively, and the corresponding recovery times for these sensors were 808, 766, and 816 s, respectively. It can be seen that the response time for the Pd-RGO-0 sensor is longer than that of the irradiated gas sensors. This is due to presence of more oxygen functional groups and the higher number of oxygen defects in the sensors irradiated with the electron beam. Thus, these materials act as favorable adsorption sites for gas molecules. Further, the Pd-RGO-500 sensor has a longer recovery time relative to that of the Pd-RGO-0 sensor. As 500 kGy of irradiation
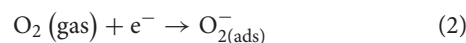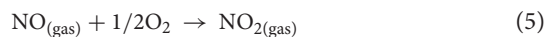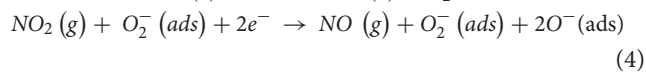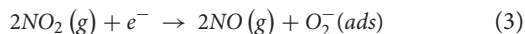
At higher temperatures, other forms of oxygen ions, specifically O^- and O^{2-}, can exist (Xu et al., 2011); however, as our sensors work at room temperature, we do not consider these species of oxygen. When NO_2 gas is introduced into the gas chamber, it interacts with the RGO surface, acting as an oxidizing gas that traps electrons and is dissociated in the form of NO, thus leaving oxygen absorbents (O_2^-). This O_2^- anion then becomes an active site to absorb NO_2 molecules. Subsequently, NO can again be converted into NO_2 after reacting with half of an O_2 molecule (Yaqoob et al., 2015).

$$2NO_2\,(g) + e^- \;\rightarrow\; 2NO\,(g) + O_2^-\,(ads) \tag{3}$$

$$NO_2\,(g) + O_2^-\,(ads) + 2e^- \;\rightarrow\; NO\,(g) + O_2^-\,(ads) + 2O^-\,(ads) \tag{4}$$

$$NO_{(gas)} + 1/2O_2 \;\rightarrow\; NO_{2(gas)} \tag{5}$$

Chemical sensitization (CS) and the electronic effect are two important aspects of Pd-functionalization. In CS, NO_2 initially adsorbs onto the surfaces of Pd, dissociates, and then spills over onto the RGO (Kim et al., 2011). Moreover, due to the difference in the work functions of Pd [$\sim$5.12 eV (Kim et al., 2017)] and RGO [$\sim$4.75 eV (Abideen et al., 2015)], the electron transfer from RGO to Pd results in the formation of a hole-accumulation layer in RGO. After NO_2 adsorption and the capture of electrons, the thickness of the hole-accumulation layer in the RGO increases, leading to a decrease in the resistance and the appearance of a response in the sensor (Wang et al., 2015).

Several effects are associated with EBI. First, when the electrons strike the RGO surfaces, if they have enough kinetic energy they can generate surface defects. Second, electron beams can collide with oxygen molecules in the ambient environment and generate reactive and high-energy oxygen species. These reactive oxygen species combine with the RGO surfaces, generating oxygen-functional groups (Chung et al., 2013). Accordingly, it can be concluded that the changes in the sensing characteristics induced by EBI can be attributed to the modification of structural defects and oxygen-functional groups. The high-energy oxygen species may oxidize the graphene nanosheets.

After the EBI process was carried out at doses of 100 and 500 kGy, the NO_2 response was increased to 1.045 and 1.047, respectively. Therefore, the response was increased with EBI dose. In the case of the 100 kGy irradiated sensor, according to the XPS results, the amount of oxygen decreased and amount of carbon increased relative to that of the un-irradiated sensor. Therefore, enhanced gas response can be attributed to the higher amounts of oxygen vacancies or oxygen functional groups in this sensor, where more adsorption sites for the gas molecules exist. In the case of the Pd-RGO-500 sensor, XPS revealed that the oxygen content of RGO was increased due to EBI. Accordingly, the Pd-RGO-500 sensor generates numerous structural defects, as denoted in **Figure 5C** by the red circles. These sites can adsorb considerable amounts of oxygen-functional groups. For example, An et al. studied the adsorption of NO_2 on ZnO nanotubes. It was found that on a defect site, binding by NO_2 was nearly three times stronger compared to that on defect-free ZnO nanotubes (a binding energy of -0.98 eV compared to -0.30 eV). Therefore, a defective structure had a higher response level to NO_2 gas (An et al., 2008). The 500-kGy-irradiation-induced enhancement of sensing behavior is mainly related to the presence of oxygen-functional groups, which are preferential sites for the adsorption of NO_2 molecules. In addition, some non-oxygen defects such as carbon vacancies and 5-8-5 defects (Hashimoto et al., 2004) may be generated after irradiation via 500 kGy of energy with possible beneficial effects on the NO_2 response.

CONCLUSION

In summary, Pd-functionalized RGO gas sensors were synthesized by a reduction of GO by Hummer's method and the subsequent sputtering of a Pd thin layer followed by thermal treatment. The structural, morphological and NO_2 gas-sensing properties of the synthesized samples were studied after they were irradiated by a 2 MeV electron accelerator at doses of 100 and 500 kGy. The results of SEM/TEM and EDS analyses confirmed the existence of fine and dispersed Pd NPs on the surfaces of the RGO nanosheets. The highest response to NO_2 gas was observed in the Pd-RGO-500 sensor due to the presence of higher amounts of oxygen functional groups as well as higher energy defects. These results demonstrate the promotional effect of EBI, which is an eco-friendly, simple and cost-effective method to enhance the gas-sensing properties of Pd-functionalized RGO sensors, which could be applied to other sensing materials in the near future.

DATA AVAILABILITY

The raw data supporting the conclusions of this manuscript will be made available by the authors, without undue reservation, to any qualified researcher.

AUTHOR CONTRIBUTIONS

MC, JB, and WO carried out the experiments. AM prepared a draft of the manuscript. HK and SK supervised the experiments and finalized the manuscript.

FUNDING

REFERENCES

Abideen, Z. U., Katoch, A., Kim, J.-H., Kwon, Y. J., Kim, H. W., and Kim, S. S. (2015). Excellent gas detection of ZnO nanofibers by loading with reduced graphene oxide nanosheets. *Sens. Actuators B Chem.* 221, 1499–1507. doi: 10.1016/j.snb.2015.07.120

An, W., Wu, X., and Zeng, X. C. (2008). Adsorption of O_2, H_2, CO, NH_3, and NO_2 on ZnO nanotube: a density functional theory study. *J. Phys. Chem. C* 112, 5747–5755. doi: 10.1021/jp711105d

Babitha, K. K., Priyanka, K. P., Sreedevi, A., Ganesh, S., and Varghese, T. (2014). Effect of 8 MeV electron beam irradiation on the structural and optical properties of CeO_2 nanoparticles. *Mater. Charact.* 98, 222–227. doi: 10.1016/j.matchar.2014.11.004

Banhart, F., Kotakoski, J., and Krasheninnikov, A. V. (2010). Structural defects in graphene. *ACS Nano* 5, 26–41. doi: 10.1021/nn102598m

Bas, S. Z. (2015). Gold nanoparticle functionalized graphene oxide modified platinumelectrode for hydrogen peroxide and glucose sensing. *Mater. Lett.* 150, 20–23. doi: 10.1016/j.matlet.2015.02.130

Brun, M., Berthet, A., and Bertolini, J. C. (1999). XPS, AES and Auger parameter of Pd and PdO. *J. Electron Spectros. Relat. Phenomena* 104, 55–60. doi: 10.1016/S0368-2048(98)00312-0

Brunet, J., Talazac, L., Battut, V., Pauly, A., Blanc, J. P., Germain, J. P., et al. (2001). Evaluation of atmospheric pollution by two semiconductor gas sensors. *Thin Solid Films* 391, 308–313. doi: 10.1016/S0040-6090(01)01001-X

Chen, X., Huang, Y., Zhang, X., Li, C., Chen, J., and Wang, K. (2015). Graphene supported ZnO/CuO flowers composites as anode materials for lithium ion batteries. *Mater. Lett.* 152, 181–184. doi: 10.1016/j.matlet.2015.03.136.

Choi, S.-W., Jung, S.-H., and Kim, S.-S. (2011). Significant enhancement of the NO_2 sensing capability in networked SnO_2 nanowires by Au nanoparticles synthesized via γ-ray radiolysis. *J. Hazard. Mater.* 193, 243. doi: 10.1016/j.jhazmat.2011.07.053

Choi, S.-W., Katoch, A., Sun, G.-J., Kim, J.-H., Kim, S.-H., and Kim, S. S. (2014). Dual functional sensing mechanism in SnO_2-ZnO core–shell nanowires. *ACS Appl. Mater. Interfaces* 6, 8281–8287. doi: 10.1021/am501107c

Chung, M. G., Kim, D. H., Lee, H. M., Kim, T., Choi, J. H., Seo, D. K., et al. (2013). Highly sensitive NO_2 gas sensor based on ozone treated graphene. *Sens. Actuators B Chem.* 166-167, 172–176. doi: 10.1016/j.snb.2012.02.036

Craciun, M. F., Khrapach, I., Barnes, M. D., and Russo, S. (2013). Properties and applications of chemically functionalized graphene. *J. Phys. Condes. Matter* 25:423201. doi: 10.1088/0953-8984/25/42/423201

Du, H., Xie, G., Su, Y., Tai, H., Du, X., Yu, H., et al. (2019). A new model and its application for the dynamic response of RGO resistive gas sensor. *Sensors* 19:889. doi: 10.3390/s19040889

Hareesh, K., Joshi, R. P., Dahiwale, S. S., Bhoraskar, V. N., and Dhole, S. D. (2016). 6 MeV energy electron beam assisted synthesis of Ag–rGO nanocomposite and its photocatalytic activity. *Mater. Lett.* 164, 35–38. doi: 10.1016/j.matlet.2015.10.129

Hashimoto, A., Suenaga, K., Gloter, A., Urita, K., and Iijima, S. (2004). Direct evidence for atomic defects in graphene layers. *Nature* 430, 870–873. doi: 10.1038/nature02792

Huang, J., Wu, Y., Gu, C., Zhai, M., Yu, K., Yang, M., et al. (2010). Large-scale synthesis of flowerlike ZnO nanostructure by a simple chemical solution route and its gas-sensing property. *Sens. Actuators B Chem.* 146, 206–212. doi: 10.1016/j.snb.2010.02.021

Huang, Q., Wei, W., Yan, Q., Wu, C., and Zhu, X. (2015). A facile and green method for synthesis of $rGO@SiO_2@FeOOH@Ag$ nanocomposite as efficient surface enhanced Raman scattering (SERS) platforms. *Mater. Lett.* 152, 203–206. doi: 10.1016/j.matlet.2015.03.117

Hummers, W. S., and Offeman, R. E. (1958). Preparation of graphitic oxide. *J. Am. Chem. Soc.* 80:1339. doi: 10.1021/ja01539a700

Huo, D., He, J., Li, H., Yu, H., Shi, T., Feng, Y., et al. (2014). Fabrication of Au@Ag core-shell NPs as enhanced CT contrast agents with broad antibacterial properties. *Colloids Surf. B Biointerfaces* 117, 29–35. doi: 10.1016/j.colsurfb.2014.02.008

Jin, E., He, J., Sheng, K., Zhang, Z., Shi, G., and Zheng, Q. (2013). Electron-irradiation-induced reinforcement of reduced graphene oxide papers. *Acta Mater.* 61, 6466–6473. doi: 10.1016/j.actamat.2013.07.025

Jung, D., Cho, S. G., Moon, T., and Sohn, H. (2016). Fabrication and characterization of porous silicon nanowires. *Electron. Mater. Lett.* 12, 17–23. doi: 10.1007/s13391-015-5409-y

Kang, M., Lee, D. H., Kang, Y.-M., and Jung, H. (2015). Electron beam irradiation dose dependent physico-chemical and electrochemical properties of reduced graphene oxide for supercapacitor. *Electrochim. Acta* 184, 427–435. doi: 10.1016/j.electacta.2015.10.053

Karimipour, M., and Molaei, M. (2016). Red florescent Ag_2S-CdS hybrid nanoparticles prepared by a one pot and rapid microwave method. *Electron. Mater. Lett.* 12, 205–210. doi: 10.1007/s13391-015-5278-4

Kiani, M. J., Akbari, E., Kooshkaki, F. R., and Zeinalinezhad, A. (2016). Analytical investigation of carrier concentration effect on one-dimensional graphene nanoscroll. *Electron. Mater. Lett.* 12, 219–223. doi: 10.1007/s13391-015-5352-y

Kim, H., Park, S., Jin, C., and Lee, C. (2011). Enhanced gas sensing properties of p-type TeO_2 nanorods functionalized with Pd. *Nano* 6, 455–460. doi: 10.1142/S1793292011002858

Kim, J., Oh, E., Yang, Y., and Yu, D. (2016). Bias dependent photocurrent characteristics of copper sulfide single nanowires. *J. Korean Phys. Soc.* 69, 202–206. doi: 10.3938/jkps.69.202

Kim, J.-H., Kim, H. W., and Kim, S. S. (2017). Ultra-sensitive benzene detection by a novel approach: core-shell nanowires combined with the Pd-functionalization. *Sens. Actuators B Chem.* 239, 578–585. doi: 10.1016/j.snb.2016.08.071

Kim, J. H., Lee, J. H., Mirzaei, A., Kim, H. W., and Kim, S. S. (2018). SnO_2 (n)-NiO (p) composite nanowebs: gas sensing properties and sensing mechanisms. *Sensors and Actuators B Chem.* 258, 204–214. doi: 10.1016/j.snb.2017.11.063

Kim, T. U., Gang, M. G., Kim, J. A., Moon, J. H., Kim, D. G., Kim, S. H., et al. (2016). The study of light waveguide effects on ZnO nanorod arrays. *Electron. Mater. Lett.* 12, 224–231. doi: 10.1007/s13391-015-5324-2

Krasheninnikov, A. V., and Banhart, F. (2007). Engineering of nanostructured carbon materials with electron or ion beams. *Nat. Mater.* 6, 723–733. doi: 10.1038/nmat1996

Kwon, S.-N., Jung, C.-H., and Na, S.-I. (2016). Electron-beam-induced reduced graphene oxide as an alternative hole-transporting interfacial layer for high-performance and reliable polymer solar cells. *Org. Electron.* 34, 67–74. doi: 10.1016/j.orgel.2016.04.008

Kwon, Y. J., Cho, H. Y., Na, H. G., Lee, B. C., Kim, S. S., and Kim, H. W. (2014). Improvement of gas sensing behavior in reduced graphene oxides by electron-beam irradiation. *Sens. Actuators B Chem.* 203, 143–149. doi: 10.1016/j.snb.2014.06.025

Kwon, Y. J., Na, H. G., Kang, S. Y., Choi, M. S., Bang, J.-H., Kim, T. W., et al. (2017). Attachment of Co_3O_4 layer to SnO_2 nanowires for enhanced gas sensing properties. *Sens. Actuators B Chem.* 239, 180–192. doi: 10.1016/j.snb.2016.07.177

Lee, H., Lee, C.-R., Ahn, H.-K., Kim, J. S., and Ryu, M.-R. (2016). Emission characteristics of shape-engineered InAs/InAlGaAs quantum dots subjected to thermal treatments. *J. Korean Phys. Soc.* 69, 85–90. doi: 10.3938/jkps.69.85

Lin, Y. K., and Hsu, Y. J. (2013). "Preparation of $M@Cu_2O$ (M = Au, Ag, Pd) core-shell nanocrystals by a facile citrate-chelating approach," in *224th ECS Meeting*, San Francisco, CA: The Electrochemical Society.

Lu, X., Dou, H., Gao, B., Yuan, C., Yang, S., Hao, L., et al. (2011). A flexible graphene/multiwalled carbon nanotube film as a high performance electrode material for supercapacitors. *Electrochim. Acta* 56, 5115–5121. doi: 10.1016/j.electacta.2011.03.066

Meang, W. J., Seo, J., Ahn, Y., and Son, J. Y. (2016). Magnetic force microscopy of conducting nanodots in NiO thim films. *Electron. Mater. Lett.* 12, 251–254. doi: 10.1007/s13391-015-5260-1

Mirzaei, A., Kwon, Y. J., Wu, P., Kim, S. S., and Kim, H. W. (2018). Converting the conducting behavior of graphene oxides from n-type to p-type via electron-beam irradiation. *ACS Appl. Mater. Interfaces* 10, 7324–7333. doi: 10.1021/acsami.7b16458

Mirzaei, A., Park, S., Sun, G. J., Kheel, H., Lee, C., and Lee, S. (2016). Fe_2O_3/Co_3O_4 composite nanoparticle ethanol sensor. *J. Korean Phys. Soc.* 69, 373–380. doi: 10.3938/jkps.69.373

Paredes, J. I., Rodil, S. V., Alonso, A. M., and Tascon, J. M. D. (2008). Graphene oxide dispersions in organic solvents. *Langmuir* 24, 10560–10564. doi: 10.1021/la801744a

Pham, V. H., Cuong, T. V., Hur, S. H., Oh, E., Kim, E. J., Shin, E. W., et al. (2011). Chemical functionalization of graphene sheets by solvothermal reduction of a graphene oxide suspension in N-methyl-2-pyrrolidone. *J. Mater. Chem. A* 21:3371. doi: 10.1039/C0JM02790A

Smith, B. W., and Luzzi, D. E. (2001). Electron irradiation effects in single wall carbon nanotubes. *J. Appl. Phys.* 90:3509. doi: 10.1063/1.1383020

Su, Y., Xie, G., Chen, J., Du, H., Zhang, H., Yuan, Z., et al. (2016). Reduced graphene oxide–polyethylene oxide hybrid films for toluene sensing at room temperature. *RSC Adv.* 6, 97840–97847. doi: 10.1039/C6RA21077E

Su, Y., Xie, G., Tai, H., Li, S., Yang, B., Wang, S., et al. (2018). Self-powered room temperature NO_2 detection driven by triboelectric nanogenerator under UV illumination. *Nano Energy* 47, 316–324. doi: 10.1016/j.nanoen.2018.02.031

Su, Y., Xie, G., Wang, S., Tai, H., Zhang, Q., Du, H., et al. (2017). Novel high-performance self-powered humidity detection enabled by triboelectric effect. *Sens. Actuators B. Chem.* 251, 144–152. doi: 10.1016/j.snb.2017.04.039

Terrones, H., Lv, R., Terrones, M., and Dresselhaus, M. S. (2012). The role of defects and doping in 2D graphene sheets and 1D nanoribbons. *Rep. Prog. Phys.* 75:062501. doi: 10.1088/0034-4885/75/6/062501

Tola, P. S., Kim, D. J., Phan, T. L., Liu, C., and Lee, B. W. (2016). Magnetic properties and magnetocaloric effect of $LaMnO_3$ nanoparticles prepared by using the sol-gel method. *J. Korean Phys. Soc.* 69, 65–71. doi: 10.3938/jkps.69.65

Tran, Q. T., Hoa, H. T. M., Yoo, D. H., Cuong, T. V., Hur, S. H., and Chung, J. S. (2014). Reduced graphene oxide as an over-coating layer on silver nanostructures for detecting NH_3 gas at room temperature. *Sens. Actuators B Chem.* 194, 45–50. doi: 10.1016/j.snb.2013.12.062

Truong, N. T. N., and Park, C. (2016). Synthesis and characterization of tin disulfide nanocrystals for hybrid bulk hetero-junction solar cell applications. *Electron. Mater. Lett.* 12, 308–314. doi: 10.1007/s13391-015-5266-8

Uddin, A. S. M. I., and Chung, G. S. (2014). Synthesis of highly dispersed ZnO nanoparticles on graphene surface and their acetylene sensing properties. *Sens. Actuators B Chem.* 205, 338–344. doi: 10.1016/j.snb.2014.09.005

Wang, J., Kwak, Y., Lee, I.-Y., Maeng, S., and Kim, G.-H. (2012). Highly responsive hydrogen gas sensing by partially reduced graphite oxide thin films at room temperature. *Carbon* 50, 4061–4067. doi: 10.1016/j.carbon.2012.04.053

Wang, J., Rathi, S., Singh, B., Lee, I., Maeng, S., Joh, H.-I., et al. (2015). Dielectrophoretic assembly of Pt nanoparticle-reduced graphene oxide nanohybrid for highly-sensitive multiple gas sensor. *Sens. Actuators B Chem.* 220, 755–761. doi: 10.1016/j.snb.2015.05.133

Xu, Z., Chen, L., Li, J., Wang, R., Qian, X., Song, X., et al. (2011). Oxidation and disorder in few-layered graphene induced by the electron-beam irradiation. *Appl. Phys. Lett.* 98, 1183112. doi: 10.1063/1.3587798

Yan, W. M., Wei, Z., En, Z. D., An, L. S., Xing, M. W., Wei, T. Z., et al. (2014). CeO_2 hollow nanospheres decorated reduced graphene oxide composite for efficient photocatalytic dye-degradation. *Mater. Lett.* 137, 229–232. doi: 10.1016/j.matlet.2014.08.128

Yang, G., Lee, C., Kim, J., Ren, F., and Pearton, S. J. (2013). Flexible graphene-based chemical sensors on paper substrates. *Phys. Chem. Chem. Phys.* 15, 1798–1801. doi: 10.1039/c2cp43717a

Yaqoob, U., Phan, D.-T., Uddin, A. S. M. I., and Chung, G.-S. (2015). Highly flexible room temperature NO_2 sensor based on MWCNTs-WO_3 nanoparticles hybrid on a PET substrate. *Sens. Actuators B Chem.* 221, 760–768. doi: 10.1016/j.snb.2015.06.137

Yeung, C. S., Liu, L. V., and Wang, Y. A. (2008). Adsorption of small gas molecules onto Pt-doped single-walled carbon nanotubes. *J. Phys. Chem. C* 112, 7401–7411. doi: 10.1021/jp0753981

Yu, H., Xu, P., Lee, D. W., and Li, X. (2013). Porous-layered stack of functionalized AuNP–rGO (gold nanoparticles–reduced graphene oxide) nanosheets as a sensing material for the micro-gravimetric detection of chemical vapor. *J. Mater. Chem. A* 1, 4444–4450. doi: 10.1039/c3ta01401k

Zhang, Q., Xie, G., Xu, M., Su, Y., Tai, H., Du, H., et al. (2018). Visible light-assisted room temperature gas sensing with ZnO-Ag heterostructure nanoparticles. *Sens. Actuators B. Chem.* 259, 269–281. doi: 10.1016/j.snb.2017.12.052